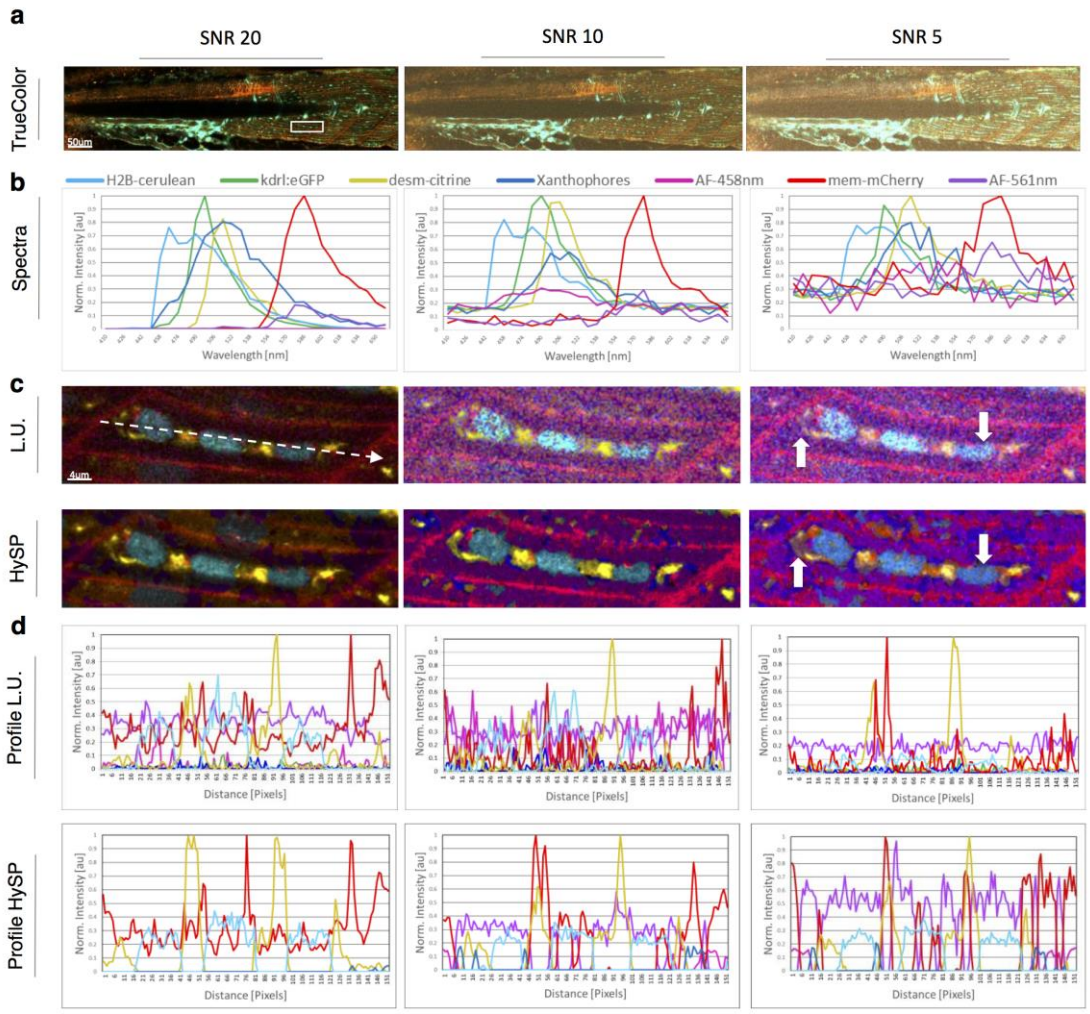

Supplementary Figure 1

Comparison of HySP and linear unmixing under different signal-to-noise ratios (SNRs).

(**a**) TrueColor images of 32 channel datasets of zebrafish labeled with H2B-Cerulean, kdrl:eGFP, Desm-Citrine, Xanthophores, membrane-mCherry as well as Autofluorescence at 458nm and 561nm. The original dataset (SNR 20) was digitally degraded by adding noise and decreasing signal down to SNR 10 and to SNR 5. (**b**) Normalized spectra used for non-weighted linear unmixing. Spectra were identified on each sample from anatomical regions known to contain only the specific label. For example Xanthophore's spectrum was collected in dorsal area, H2B-Cerulean's from fin, kdrl:eGFP's intramuscularly. Linear unmixing results were optimized over multiple iteration of unmixing regions combinations. The same regions were then used for all three datasets. The same legend and color coding is used through the entire figure. (**c**) Processed zoomed-in region (box in (a)) for linear unmixing and HySP. The comparison shows three nuclei belonging to muscle fiber. At higher SNR (20 and above) both linear unmixing and HySP results are accurate. Lowering SNR, however, affects the linear unmixing more than the phasor. This can improve unmixing of labels in volumetric imaging of biological samples, where generally SNR decreases with depth and explains the differences in Figure 2e,f, Supp. Figure 6, Supp. Figure 7e,f and Supp. Figure 9. The key advantage of HySP, in this SNR comparison, is the spectral denoising in Fourier space (Supplementary Discussion 3). (**e**) Intensity profile (dashed arrow in (c)) comparison shows the improvement of HySP at low SNR. Under decreased SNR H2B-Cerulean (cyan) and Desm-Citrine (yellow) (solid arrows in (c)) are consistently identified in HySP while they are partially mislabeled in linear unmixing. For example, some noisy are identified as kdrl:eGFP (green) while, anatomically no vasculature is present in this region of interest.

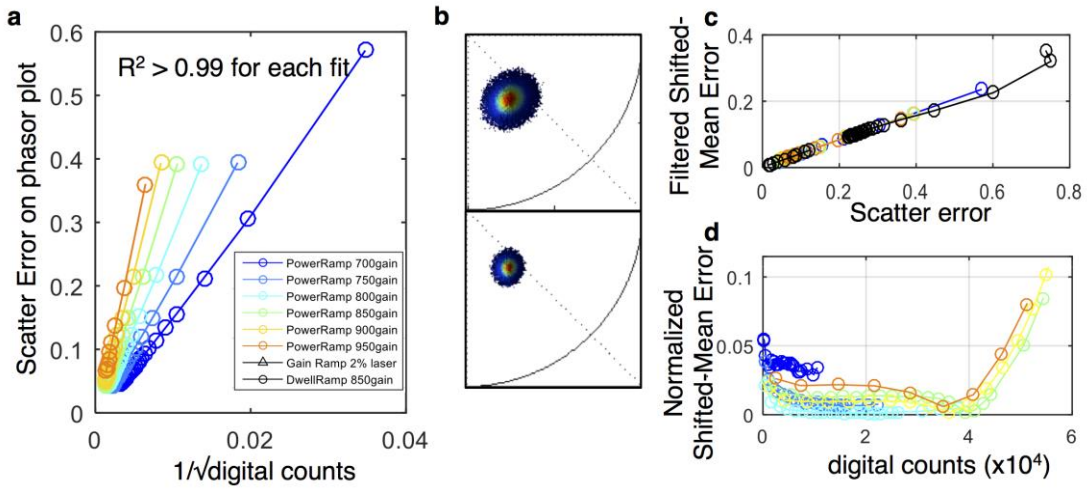

Supplementary Figure 2

Errors on hyper-spectral phasor plot.

(**a**) *scatter error* scales inversely as the square root of the total *digital counts*. Scatter error also depends on the Poissonian noise in the recording. R-squared statistical method is used to confirm linearity with the reciprocal of square root of counts. The slope is a function of the detector gain used in acquisition showing the counts-to-scatter error dynamic range is inversely proportional to the gain. Lower gains produce smaller scatter error at lower intensity values. The legend is applicable to all parts of the figure. (**b**) Denoising in the phasor space reduces the scatter error without affecting the location of expected values ($z_e(n)$) on the phasor plot. (**c**) Denoised scatter error linearly depends on the scatter error without filtering, irrespective of the acquisition parameters. The slope is determined by the filter size (3x3 here). (**d**) Denoising does not affect normalized *shifted-mean* errors since the locations of $z_e(n)$'s on the phasor plot remain unaltered due to filtering (d). In this case one filtering was applied.

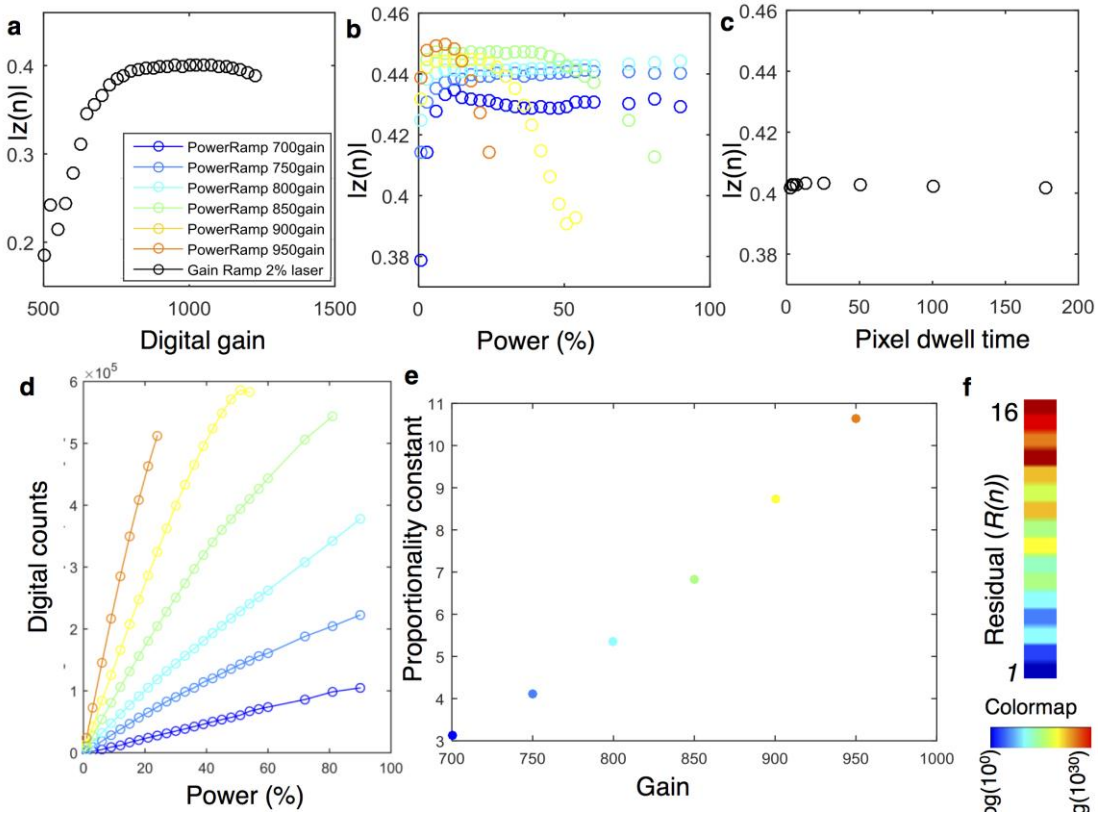

Supplementary Figure 3

Sensitivity of phasor point.

(**a,b,c**) |Z(n)| remains nearly constant for different imaging parameters. Legend applies to (a,b,c,d,e). (**d**) Total digital counts as a function of laser power. (**e**) Proportionality constant in eq. 2 depends on the gain. (**f**) Relative magnitudes of residuals (*R(n)*) on phasor plots at harmonics 1 to 16, shows that harmonics *n =1 and 2* are sufficient for unique representation of spectral signals.

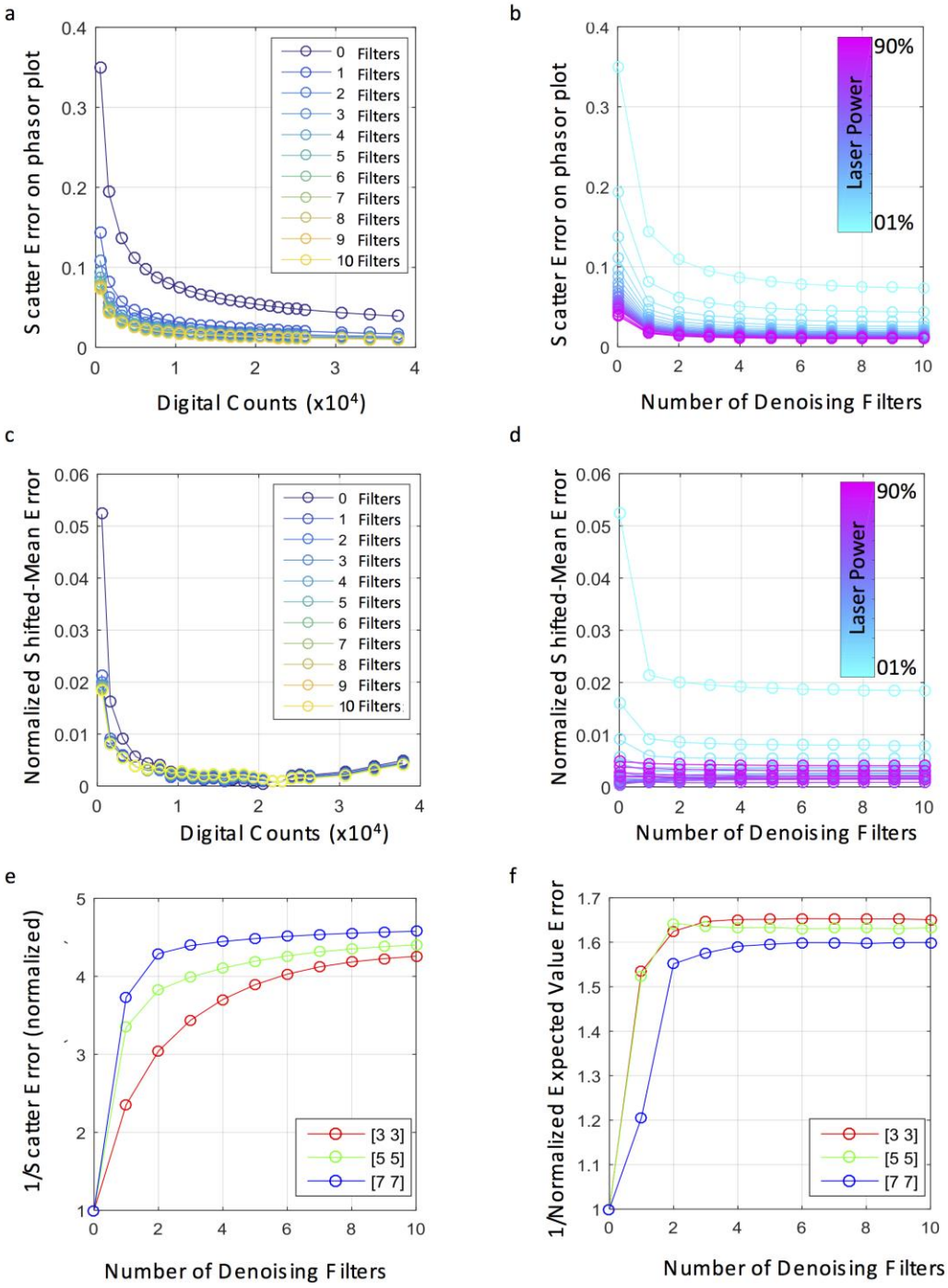

Supplementary Figure 4

Effect of phasor space denoising on scatter error and shifted-mean error.

(**a**) Scatter Error as a function of digital counts for different numbers of denoising filters with 3 by 3 mask. Data origin is fluorescein dataset acquired at gain 800 (Supp. Table 2). (**b**) Scatter Error as a function of number of denoising filters with 3 by 3 mask for different laser powers. (**c**) Shifted-Mean Error as a function of digital counts for different number of denoising filters with 3 by 3 mask. Data origin is fluorescein dataset acquired at gain 800. (**d**) Shifted-Mean Error as a function of number of filters with 3 by 3 mask for different laser powers. (**e**) Relative change of Scatter Error as a function of number of denoising filters applied for different mask sizes. (**f**) Relative change of Shifted-Mean Error as a function of number of filters applied for different mask sizes.

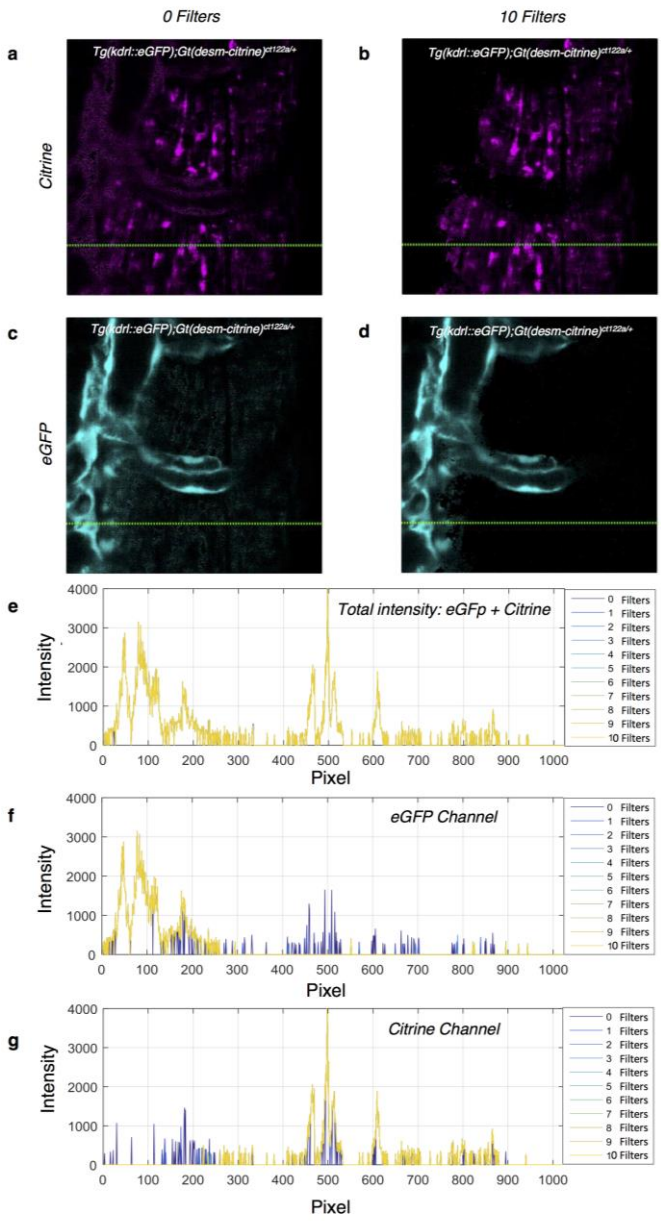

Supplementary Figure 5

Effect of phasor space denoising on image intensity.

(**a,b**) HySP processed Citrine channel of a dual labeled eGFP-Citrine sample (132.71um x 132.71um) before and after filtering in phasor space. (**c,d**) HySP processed eGFP channel of the sample in (a,b) before and after filtering in phasor space. (**e**) Total intensity profile of the green line highlighted in (a,b,c,d) for different number of denoising filters. Intensity values are not changing. (**f**) eGFP channel intensity profile of green line highlighted in (a,b,c,d) for different number of denoising filters. (**g**) Citrine channel intensity profile of green line highlighted in (a,b,c,d) for different number of denoising filters.

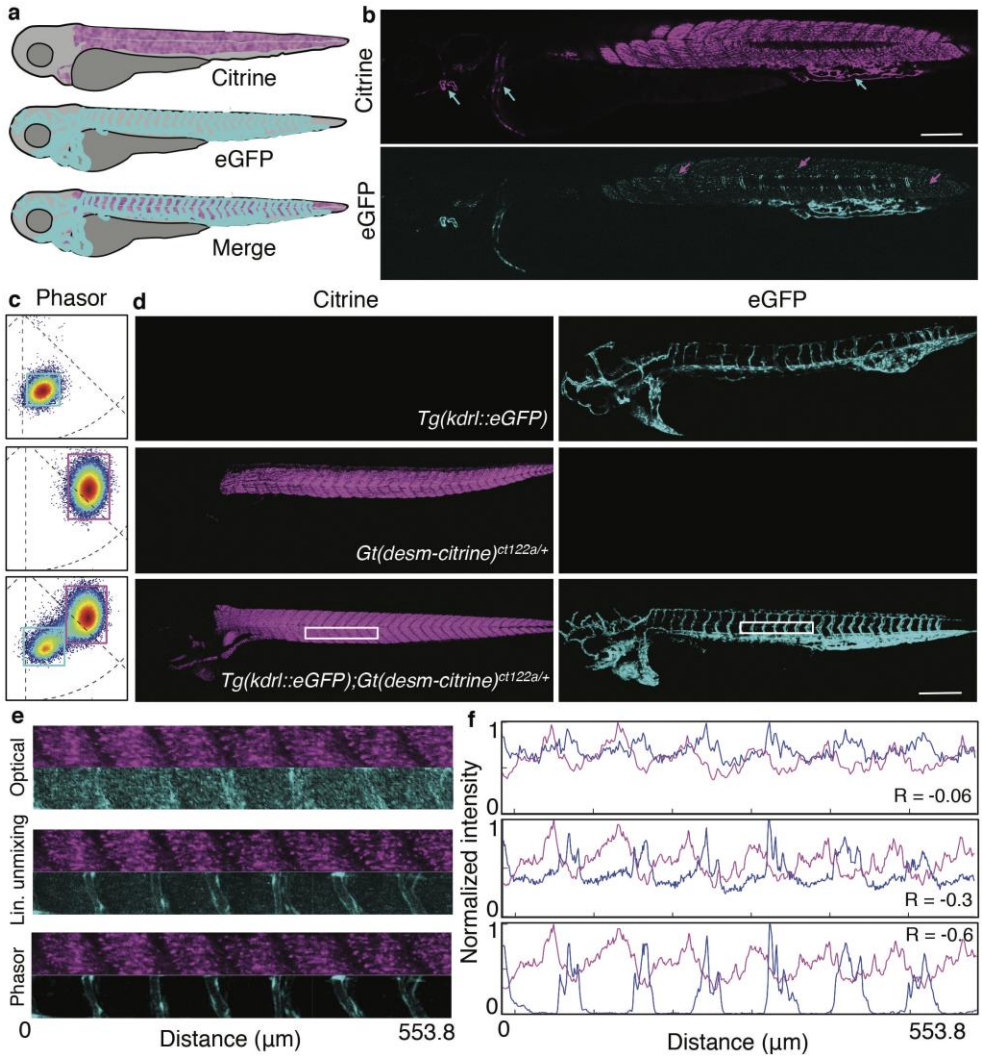

Supplementary Figure 6

Phasor analysis for unmixing hyper-spectral fluorescent signals *in vivo*.

(**a**) Schematic of the expression patterns of Citrine (skeletal muscles) and eGFP (endothelial tissue) in transgenic zebrafish lines *Gt(desm-citrine)*$^{ct122a/+}$ and *Tg(kdrl:eGFP)* respectively. (**b**) Conventional optical filter separation for *Gt(desm-citrine)*$^{ct122a/+}$ *Tg(kdrl:eGFP).* Using emission bands on detector of spectrally overlapping fluorophores (eGFP and citrine) cannot overcome the problem of bleed-through of signal in respective channels. Arrows indicate erroneous detection of eGFP or Citrine expressions in the other channel. Scale bar, 200µm. (**c**) Phasor plots showing spectral fingerprints (scatter densities) for Citrine and eGFP in individually expressed embryo and double transgenic. The individual Citrine and eGFP spectral fingerprints remain preserved in the double transgenic line. (**d**) Maximum intensity projection images reconstructed by mapping the scatter densities from phasor plot to the original volume. eGFP and Citrine fingerprints can cleanly distinguish the skeletal muscles from interspersed blood vessels (endothelial tissue), within the same anatomical region of the embryo, in both single and double transgenic lines. Scale bar 300µm. Embryos imaged around 72 hours post fertilization. (**e,f**) HySP analysis outperforms optical separation and linear unmixing in distinguishing spectrally overlapping fluorophores *in vivo*. (e) Maximum intensity projection images of the region in *Tg(kdrl:eGFP);Gt(desm-citrine)*$^{ct122a/+}$ shown in (d) compares the signal for eGFP and Citrine detected by optical separation, linear unmixing and phasor analysis. (f) Corresponding normalized intensity profiles along the width (600 pixels, 553.8µm) of the image integrated over a height of 60 pixels. Correlation values (R) reported for the three cases show the lowest value for HySP analysis, as expected by the mutually exclusive expressions of the two proteins.

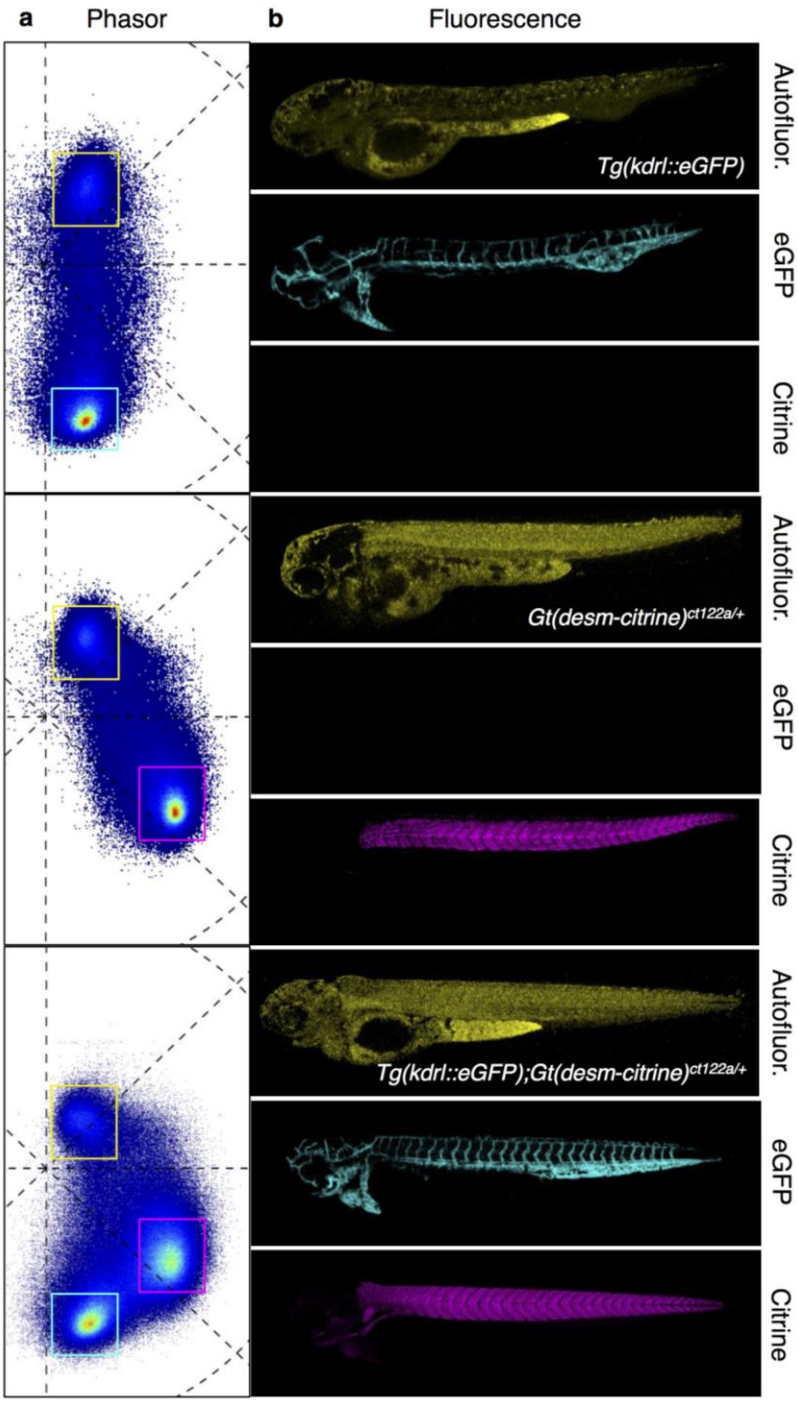

Supplementary Figure 7

Autofluorescence identification and removal in phasor space.

(**a**) Phasor plots showing spectral fingerprints (scatter densities) for citrine, eGFP and autofluorescence allow simple identification of intrinsic signal. (**b**) Maximum intensity projection images reconstructed by mapping the scatter densities from phasor plot to the original volume. Autofluorescence has a broad fingerprint that can effectively be treated as a fluorescent signature and saved as a channel. Embryos imaged around 72 hours post fertilization.

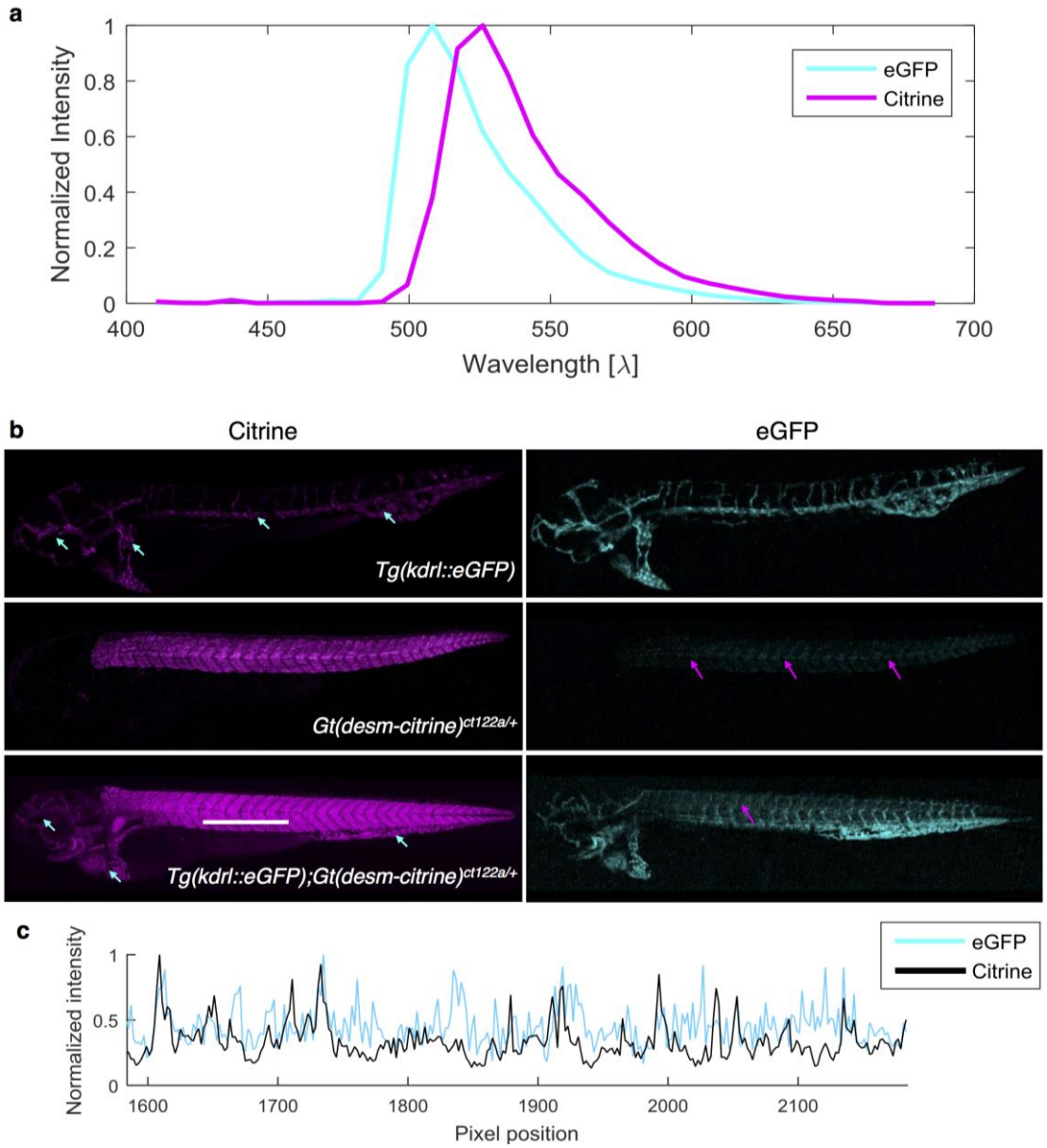

Supplementary Figure 8

Optical separation of eGFP and citrine.

(a) Spectra of citrine (peak emission 529nm, skeletal muscles) and eGFP (peak emission 509nm, endothelial tissue) measured using confocal multispectral lambda mode in transgenic zebrafish lines *Gt(desm-citrine)*$^{ct122a/+}$ and *Tg(kdrl:eGFP)* respectively. (**b**) Conventional optical separation (using emission bands on detector) of spectrally close fluorophores (eGFP and citrine) cannot overcome the problem of bleed-through of signal in respective channels. Arrows indicate erroneous detection of eGFP or citrine expressions in the other channel. Scale bar 300µm. (**c**) Normalized intensity profiles along the line (600 pixels, 553.8µm) in panel (a)

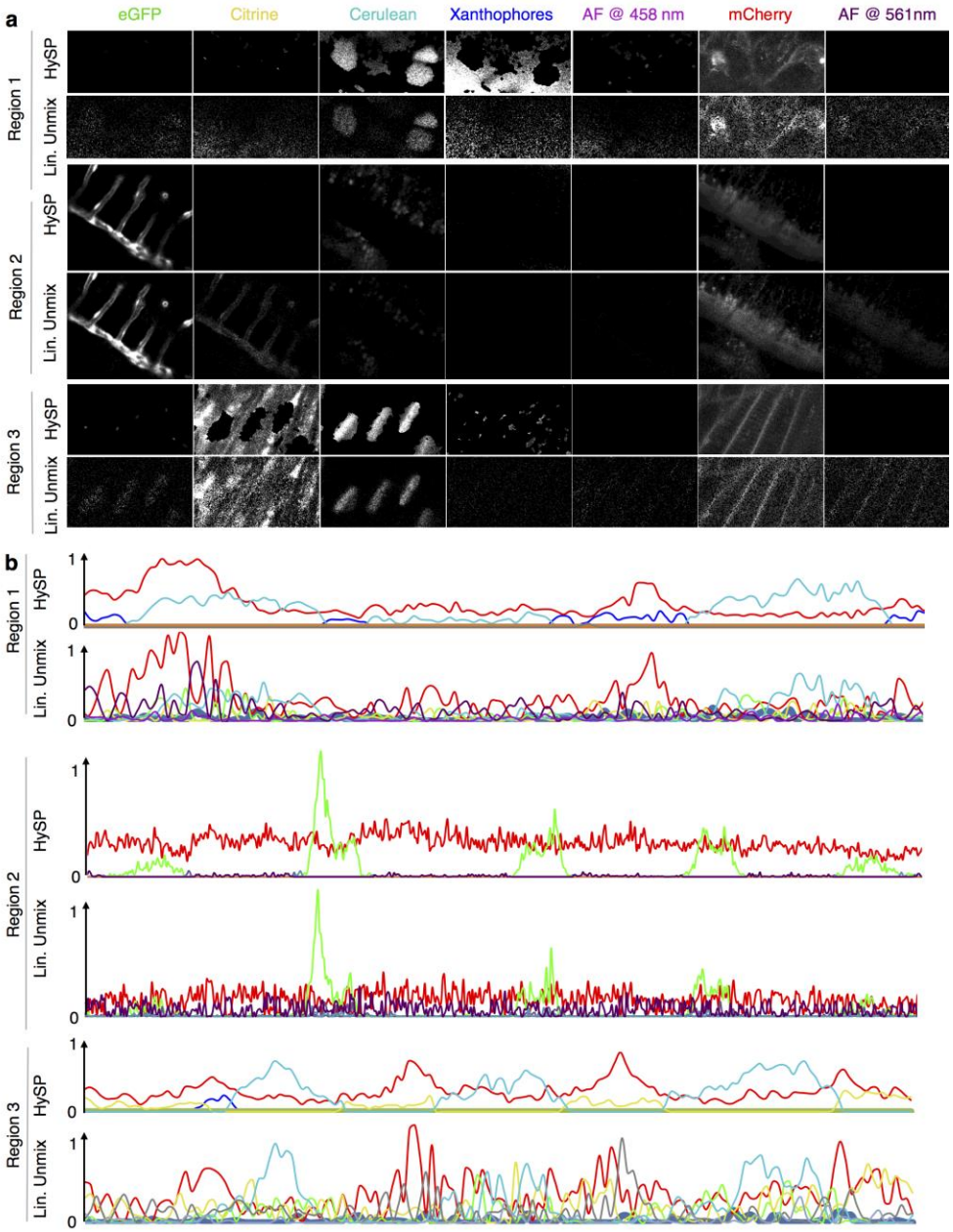

Supplementary Figure 9

Comparison of HySP and linear unmixing in resolving 7 fluorescent signals.

(a) Gray scale images from different optical sections, same as the ones used in Fig 2 (Regions 1-3), comparing the performance of HySP analysis and linear unmixing. (**b**) Normalized intensity plots for comparison of HySP analysis and linear unmixing. Similar to the corresponding panels in Fig. 2f, the x-axes denote the normalized distance and y-axes in all graphs were normalized to the value of maximum signal intensity among the 7 channels to allow relative comparison. The panels show all intensity profiles for 7 channels in the respective images.

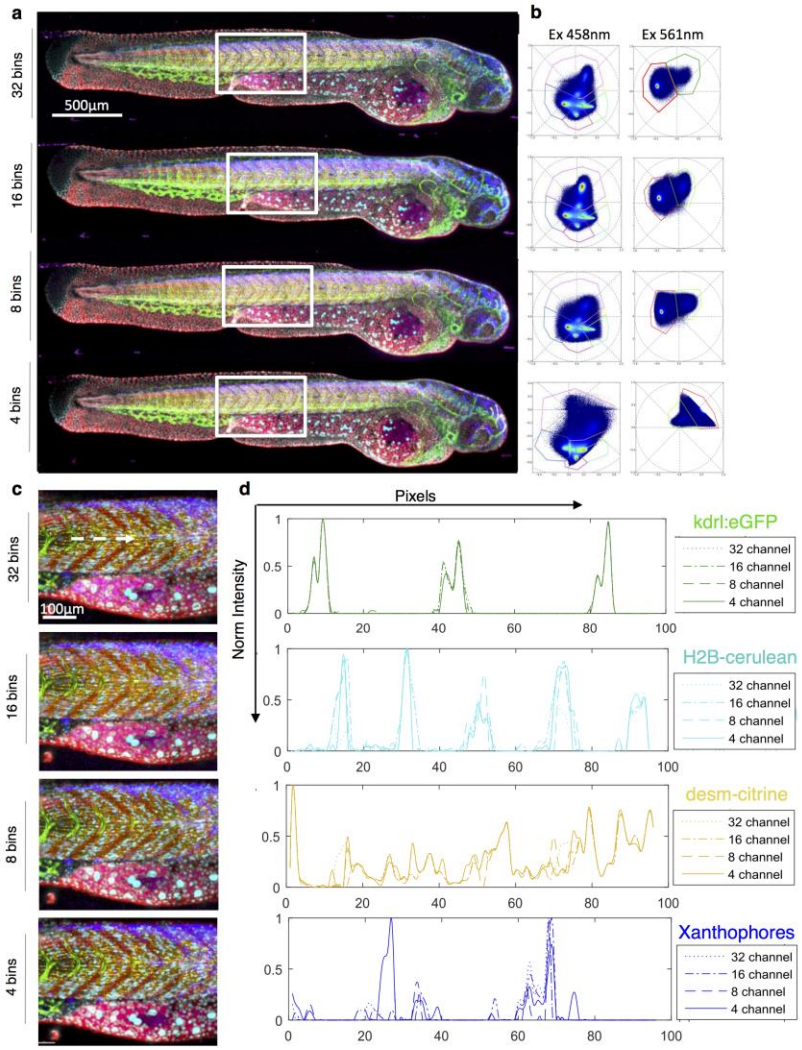

Supplementary Figure 10

Effect of binning on HySP analysis of 7 *in vivo* fluorescent signals.

(a) The original dataset acquired with 32 channels is computationally binned sequentially to 16, 8 and 4 channels to understand the limits of HySP in unmixing the selected fluorescence spectral signatures. The binning does not produce visible deterioration of the unmixing. White square area is used for zoomed comparison of different bins. (b) Hyper-spectral phasor plots at 458nm and 561nm excitation. Binning of data results in shorter phasor distances between different fluorescent spectral fingerprints. Clusters, even if closer, are still recognizable. (c) Zoomed-in comparison of embryo trunk (box in (a)). Differences for HySP analysis for the same dataset at different binning values are still subtle to the eye. One volume is chosen for investigating intensity profiles (white dashed arrow). (d) Intensity profiles for kdrl:eGFP, H2B-Cerulean, Desm-Citrine and Xanthophores at different binning for summed intensities of a volume of 26.60x0.27x20.00 µm (white dashed arrow (c)). The effects of binning are now visible. For kdrl:eGFP the unmixing is not excessively deteriorated by the binning. Same result for H2B-Cerulean. Desm-Citrine and Xanthophores seems to be more affected by binning. This result suggests that, in our case of zebrafish embryo with 7 separate spectral fingerprints acquired sequentially using two different lasers, it is possible to use 4 bins at the expense of a slight deterioration of the unmixing.

Supplementary Table 1 : Parameters for Fluorescein imaging

	Gain (A.U.)	488nm laser power (%)	Pixel dwell time (µs)
Experiment 1	500-1250 in steps of 25	2	6.3
Experiment 2	700	1-60 in steps of 3	6.3
Experiment 3	750	1-60 in steps of 3	6.3
Experiment 4	800	1-21 in steps of 3	6.3
Experiment 5	850	1-21 in steps of 3	6.3
Experiment 6	900	1-21 in steps of 3	6.3
Experiment 7	950	1-21 in steps of 3	6.3
Experiment 8	850	21	2.55 – 177.32 in steps dictated by controlling software

Supplementary Table 2 : Proportionality constant for curves to calculate scatter error on phasor plot

Gain (A.U.)	Slope	$\|z(n)\|$	Proportionality constant
700	1.35	0.43	3.14
750	1.8	0.437	4.12
800	2.34	0.437	5.36
850	3.03	0.443	6.83
900	3.89	0.446	8.72
950	4.79	0.45	10.65

Supplementary Table 3: Parameters for *in vivo* imaging. All data points are 16 bits integers.

	Zebra fish Stage [hpf*]	Imaged volume (xyz/t) [pixels]	Lateral pixel (x,y resol.) [µm]	Axial section (z resol.) [µm]	Pixel dwell time [µs]	Pinhole size [µm]	Laser Power (%)
Fig 1A, Supplementary Fig. 6B,D, 8B, 7B (Tg(kdrl::eGFP);Gt(desm-citrine)$^{ct122a/+}$**), Supplementary Video 1, 2, 11**	72	3584x768x45x32x1	0.92	5.0	5.09	180	0.3 @488nm
Supplementary Fig. 6D, 8B, 7B (Gt(desm-citrine)$^{ct122a/+}$**)**	72	1408x384x39x32x1	1.84	5.0	5.09	180	0.5 @488nm
Supplementary Fig. 6D, 8B, 7B (Tg(kdrl::eGFP)**)**	72	1408x384x40x32x1	1.84	5.0	5.09	180	0.9 @488nm
Supplementary Fig 6E,F	72	600x60x45x32x1	0.95	5.0	5.09	180	0.3 @488nm
Fig 2C, Supplementary Video 3,5, Supplementary Fig. 9	74	2560x2048x29x32x1	0.277	5.0	3.15	186	3.0 @458nm
Fig 2C, Supplementary Video 3,5, Supplementary Fig. 9	74	2560x2048x29 x32x1	0.277	5.0	3.15	186	0.3 @561nm
Supplementary Fig. 5A,B,C,D	72	1024x1024x1x32x1	0.13	1.4	3.15	70	1.0 @488nm
Fig 2A,Supplementary Fig 10 Supplementary Video 4,6	72	1664x512x55x32x1	2.076	5.0	6.50	186	3.0-5.0 @458nm
Fig 2A, Supplementary Fig 10, Supplementary Video 4,6	72	1664x512x55x32x1	2.076	5.0	6.50	186	0.18 @561nm
Fig 3b,c,d,e, Supplementary Video 7,10	24	512x512x(25-40)x32x25	0.277	2.0	2.55	601	5@950nm
Fig 3b,c,d,e, Supplementary Video 7,10	24	512x512x(25-40)x32x25	0.277	2.0	2.55	601	0.2@561nm
Fig 3b,c,d,e	24	512x512x(25-40)x32x25	0.277	2.0	2.55	150	0.2@561nm
Supplementary Video 8	30	1024x512x(15-23)x32x15	0.277	2.0	2.55	601	7@950nm
Supplementary Video 8	30	1024x512x(15-23)x32x15	0.277	2.0	2.55	150	0.6@561nm
Supplementary Video 9	25	1536x512x(13-25)x32x15	0.231	2.0	2.55	601	7@950nm
Supplementary Video 9	25	1024x512x(13-23)x32x15	0.231	2.0	2.55	150	0.45@561nm

*hpf = hours post fertilization

Supplementary Note 1

Harmonic number in phasor analysis

Typically, phasor plots have been calculated using the first or the second harmonic of the Fourier representation of the spectral profile to determine the unique spectral signatures. This is due mainly to two factors: visualization issues and deviation from the original information in the data. Visualization issues arise from the presence of branch points in the Riemannian surfaces in complex plane corresponding to representations of harmonics greater than 2. These planes are not easy to visualize in an intuitive 2 dimensional plot. Deviation from the original data can be calculated using residuals. Based on eq. 1 we calculate residuals (*ρ(n))* as the ratio of the absolute sum of all Fourier coefficients except the one corresponding to the harmonic number (*n*) of choice, to the absolute value of the n^{th} Fourier coefficient. Therefore:

$$\rho(n) = \frac{\sum_{i=0, i\neq n}^{N}\left(\langle S_i\rangle^2+\langle G_i\rangle^2\right)}{\langle S_n\rangle^2+\langle G_n\rangle^2} \quad \text{.....(14)}$$

For typical fluorescent spectra, such as the Fluorescein emission spectrum here, 1 and 2 remain the dominant harmonic numbers, as the residuals for these are at least an order of magnitude smaller than the residuals for other harmonics (Supp Fig. 2f). Further fluctuations in residual values are dependent on the exact nature of the spectrum being analyzed, in particular on the shape of the spectrum analyzed. Changing harmonic in HySP is easily implemented every time hyperspectral phasor analysis is done and allows a quick verification of the choice of the harmonic number used for any recorded spectrum.

Supplementary Note 2

Changes in Shifted-Mean of a spectrum

Phasor plot relies on normalized spectrum of a pixel to determine the coordinates. However, both the saturation of signal and very low photon counts (low signal to noise ratio (SNR)) result in non-identical normalized spectra (Fig. 1b, inset). This changes the values of |z(n)| at the extreme values of total digital counts (Fig. 1f, Supp. Fig. 3c). At low SNR the signal is indistinguishable from noise. At very high SNR, identical intensity values for several wavelengths, corresponding to saturation value on detector (Fig. 1b, inset), skew the spectrum. In either cases the phasor point moves to coordinates closer to origin leading to low values of |z(n)|. Within the constant regime (2000-44000 Digital Levels) (Fig. 1f , Supp. Fig. 2d) the values of |z(n)| are most sensitive to changes in the values of detector gain among the three parameters - namely detector gain, power and pixel dwell time (Supp Fig. 3a-c).

Supplementary Note 3

Detection mode and phasor performance

The type of detection used for measures will affect the error on phasor. In any imaging system, the number of photons emitted by a dye during a time interval is a stochastic (Poissonian) process, where the signal scales as the average number of acquired photons (N, [15,26]) and the noise scales as $\sqrt{N}$. Typically the source of noise comprises of shot noise resulting from (i) signal light (ii) background light and (iii) dark current.

In our experiments we used analog detectors for all measures. A typical Photomultiplier Tube (PMT) can measure the pulse of electrons at the anode resulting from a photon striking at its photocathode. These pulses can be counted both individually and as an averaged photocurrent in a given interval, thereby allowing both digital (photon-counting) and analog modes of operation respectively.

In photon counting mode the Signal-to-Noise Ratio (SNR) can be approximated by:

$$SNR_{PCM} \approx \frac{I_S\,(t)^{1/2}}{\{I_s+2(I_{bg}+I_{dc})\}^{1/2}} \qquad \text{.....(15)}$$

where I_s, I_{bg} and I_{dc} are number of counts per second respectively from signal light (I_s), background light (I_{bg}) and dark current (I_{dc}) while t is the measurement time.

In analog mode the SNR has a different form and can be approximated by:

$$SNR_{ANM} \approx \frac{I_S}{\{A\,T_{noise}[I_s+2(I_{bg}+I_{dc})]\}^{1/2}} \qquad \text{.....(16)}$$

where I_s, I_{bg} and I_{dc} are number of counts per second respectively from signal light (I_s), background light (I_{bg}) and dark current (I_{dc}). T_{noise} represents the noise induced by the PMT while A depends on bandwidth of the detection system and electron charge [26,29].

From the equations above, considering t=1 second, SNR in photon counting mode should perform $(AT_{noise})^{1/2}$ times better than in analog mode. While the noise (Poissonian) from signal and background light remains the same for both analog and digital counts, shot noise from dark currents can vary in the two modes. The dark current consists of thermal electrons with a typical pulse height distribution that, in photon-counting, can be discriminated robustly from the signal using a pulse height discriminator and thus eliminated. In analog mode, the averaged pulse incorporates also the dark current leading to a higher noise. Signal to noise ratio (SNR) in the digital mode improves compared to analog mode. Additionally, photon-counting mode better performs at low signal levels, so as to avoid simultaneous arrival of two photons. Analog mode operates over a wide range of photon levels.

For the purpose of HySP, the Fourier transforms convert all photons collected across spectrum into one point in the phasor plot. In the main text we show

enhanced performance of HySP in the low SNR regimes. In the photon-counting mode, HySP performance is expected to be further enhanced due to the improved SNR compared to analog mode at low signal levels.

Supplementary Note 4

Spectral denoising in phasor space

Spectral denoising is performed by applying filters directly in phasor space. This maintains the original image resolution but improves spectral fingerprinting in the phasor plot. The filter here applied is a median filter, however other approaches are possible. For any image of a given size (n x m pixels), S and G values are obtained for every pixel, yielding 2 new 2D matrices, for S and G, with dimensions n x m. Effectively by using filtering in phasor space, we treat S and G matrices as two images. Since the initial S and G matrix entries have the same indices as the pixels in the image, the filtered matrices S* and G*, therefore, preserve the geometrical information. The advantages are two folds: first, this reduces both the *scatter error* (Supp Fig. 4a-b) and the already minimal Shifted-Mean Error (Supp Fig. 4c-d), resulting in an improved separation of distinct fluorescent proteins (Supp Fig. 5a-d). Second, denoising in (G,S) coordinates preserves geometry, intensity profile as well as the original resolution at which the images were acquired (Supp Fig. 5e-g).

Supplementary Note 5
Autofluorescence in phasor space for *in vivo* imaging

Hyperspectral phasor allows intuitive identification of fingerprints for fluorescent proteins. This is shown for commonly used fluorophores such as Citrine and eGFP but is valid also for autofluorescence. Intrinsic fluorescence is a known and common issue in *in vivo* biological imaging and can arise from multiple molecules, intra- and extra-cellularly. When represented on phasor plot as a scatter density, autofluorescence has different (S,G) coordinates compared to fluorescent proteins and creates cluster regions in different area of the plot (Supp Fig. 7a).
Effectively, phasor plot identifies autofluorescence as a separate spectral fingerprint allowing it to be treated as an independent fluorescent species (Supp Fig. 7b).

Supplementary Note 6
Multispectral volumetric time-lapse *in vivo* imaging with phasor

Hyperspectral phasor allows reduced photo-damage when performing multispectral volumetric time-lapses in vivo. The improved unmixing efficiency at decreased Signal to Noise Ratio (Supp. Fig. 1) plays a key role in tackling issues related to reduced number photons.
Generally, when multiple fluorophores are present in the sample, each fluorophore will have an optimal excitation wavelength. It is however complicated to use multiple wavelengths which are too close (e.g. 458nm-488nm-514nm for CFP, GFP, YFP) for excitation without considerably affecting the emission spectra, due to the dichroics and filters that would be required in such task. One solution is to sequentially excite a volume with each wavelength. Sequential excitation, while optimal to reduce overlapping of emission spectra, requires an extended scanning time and results in increased photo-damage and -bleaching. Additionally, extended scanning time might result in motion artifacts due to sample development. An alternative option is to excite with a single wavelength for multiple fluorophores. The disadvantage in this approach is the excitation efficiency of the lowest wavelength fluorophore will be higher than the other fluorophores in the sample. For example, at 458nm the excitation efficiency of CFP is 93%, while GFP is 62% and YFP is 10%. There is a series of factors that affect the actual number of photons emitted by each fluorophore, such as quantum yield, brightness, pH and concentration. However, in general, we observe a stronger signal from one fluorescent protein and a weak signal from another. One might want to increase laser power in an attempt to extract more photons from the weaker signal. The effects of increasing laser power above 10% for 950nm (n=2) or above 10% for 458nm (n=3), in our experiments, resulted in halted development of vasculature due to photo-toxicity. The opposite solution is to deal with lower noisier signals, allowing for correct development of the sample.
The Hyperspectral Phasor method allows for improved performance at lower SNR, hence overcoming the issue of the weaker signals. This advantage consequently carries over to 2-photon imaging where excitation efficiency is lower than 1-photon and changing laser wavelength requires few seconds.
As a consequence, the imaging time can be reduced to at least one third in the 3-fluorophore example described above.
The same approach can be applied on different color-clusters of proteins, for example one “blue” cluster CFP-GFP-YFP (excited at 458nm), a second “red” cluster mCherry-tdTomato-RFP (excited at 561nm), a third cluster with the multiple iRFPs (excited at 630nm).
We show (Supp. Video 7-10) two-photon and one-photon multicolor volumetric time-lapse imaging of multiple samples as an example of potential application with two color-clusters.